

Controlled irradiation hardening of tungsten by cyclic recrystallization

A. Mannheim, J.A.W. van Dommelen* and M.G.D. Geers

Mechanics of Materials, Mechanical Engineering, Eindhoven University of Technology, P.O. Box 513, 5600 MB Eindhoven, The Netherlands

January 18, 2019

Abstract

The economical lifetime of the divertor is a key concern for realizing nuclear fusion reactors that may solve the world's energy problem. A main risk is thermo-mechanical failure of the plasma-facing tungsten monoblocks, as a consequence of irradiation hardening induced by neutron displacement cascades. Lifetime extensions that could be carried out without prolonged maintenance periods are desired. In this work, the effects of potential treatments for extending the lifetime of an operational reactor are explored. The proposed treatments make use of cyclic recrystallization processes that can occur in neutron-irradiated tungsten. Evolution of the microstructure under non-isothermal conditions is investigated, employing a multi-scale model that includes a physically-based mean-field recrystallization model and a cluster dynamics model for neutron irradiation effects. The model takes into account microstructural properties such as grain size and displacement-induced defect concentrations. The evolution of a hardness indicator under neutron irradiation was studied. The results reveal that, for the given microstructure and under the assumed model behaviour, periodical extra heating can have a significant positive influence on controlling the irradiation hardening. For example, at 800 °C, if extra annealing at 1200 °C was applied after every 100 hrs for the duration of 1 hr, then the hardness indicator reduces from maximum 140 to below 70.

1 Introduction

In a tokamak-design nuclear fusion device, the component that receives the highest heat load (10 MW/m² for DEMO [1]) is the divertor. Monoblocks, made out of high purity tungsten, are positioned on the plasma-facing side of this component. They absorb the heat that was generated during the fusion reaction and direct it towards the cooling water. The monoblocks are actively cooled, and therefore the heat load induces a strong temperature gradient that leads to thermal stresses in the monoblock. Moreover, the tungsten is also damaged by high neutron and ion loads (leading to 15 dpa (displacements per atom) in 5 years of operation of DEMO and peak ion loads of 10²⁴ ions/m³s [1]). Hereby, the ions mainly affect the surface of the monoblock, while the neutrons affect the entire monoblock. Despite these extreme conditions, the divertor needs to have a minimum lifetime of 2 years prior to replacement for reasons of economical viability. This means that interim repairs for prolongation of the divertor lifetime are most likely needed.

The lifetime of the tungsten monoblocks under heat and neutron irradiation will depend strongly on the evolution of the strength and ductility of the material. A high hardness, which is reported for fission-neutron-irradiated tungsten [2, 3] can be associated to a high yield strength and low ductility.

The high density of displaced atoms (resulting from the continuous neutron displacement cascades that are generated by the 14.0 MeV fusion neutrons) entails a high stored energy in the

*Correspondence to J.A.W. van Dommelen. Electronic mail: j.a.w.v.dommelen@tue.nl

material. The ongoing accumulation of stored energy, in combination with sufficiently high temperatures, can lead to (repeated) dynamic recrystallization. During dynamic recrystallization, the material’s microstructure is completely renewed, from heavily defected to virtually free of lattice defects. Dynamic recrystallization can be instrumental in decreasing the material’s hardness. In [4], it was shown for steel that (strain-induced) recrystallization can lead to softening and to an improved ductility. A treatment that achieves an improved ductility and removes the accumulated lattice damage, is most likely necessary for neutron-irradiated tungsten. Although, depending on the composition, recrystallization can lead to embrittlement, under the right circumstances, it may lead to an improved ductility by regeneration of the lattice.

For most materials, recrystallization leads to an increase in ductility and a decrease in yield strength. For tungsten, the literature is divided on this point. Degradation of the ductility for post-recrystallization was reported in [5] and [6]. However, the testing temperature may have been too low in that analysis to improve the ductility (below the brittle-to-ductile transition temperature, which is reported to increase by recrystallization). On the other hand, there are also examples in literature where the ductility of tungsten increases after recrystallization, such as by Wirtz *et al.* [7], who found for several grades of tungsten a significantly improved uniform elongation and total elongation in post-recrystallization (accompanied by a lower yield strength), or [8], where fracture strains were reported of 17% and 22% prior to recrystallization and 68% after recrystallization. The impurity content of the tungsten grade may play a role in the grain boundary cohesion [9], which can affect the ductility. Recrystallization may lead to an increase in impurity concentrations at the grain boundary surfaces, because the impurities are redistributed and because the grain boundary surface density changes for a different average grain size. It was suggested that the ductility in tungsten may be determined by the presence of edge dislocations [10], but the mechanisms that control the ductility of tungsten are not properly understood, whereby the effects of grain size and cold working were not studied separately yet.

The combined effect of heat and neutron load on the microstructural evolution of tungsten were already studied in [11, 12], using multi-scale modelling. In [11], a multi-scale model was presented, consisting of a mean-field recrystallization model and a cluster dynamics model. The model was parametrized based on static recrystallization experiments [13] and the evolution of the microstructural properties (grain size distribution, defect distribution) was predicted. Cyclic neutron-induced recrystallization was predicted to occur for temperatures in the range 1000°C - 1400°C [12] for the considered microstructure, displacement damage rate and material behaviour. In addition, only a limited irradiation hardening was predicted for cyclic recrystallization [12] at high temperatures. Neutron-induced recrystallization and grain growth were also studied in [14, 15].

In this paper, the main objective is to explore the use of dedicated interim heat treatments of tungsten for manipulating the microstructure such that the divertor lifetime may be prolonged. In particular, it is studied whether temporary, periodical, extra heating can be used to keep the hardness increase below a certain level. For these non-isothermal studies, the multi-scale model that was presented in [12] is extended, employing a multitude of homogeneous equivalent media (HEMs) instead of just two HEMs, to eliminate the effects of additional parameters in the grain growth part of the model. Furthermore, because of these extensions, a reparametrization of the model is done and it is discussed which recrystallization experiments would be valuable in order to further improve model predictions.

2 Method

2.1 Multi-scale approach

A multi-scale model is used to describe microstructural evolution under neutron loading for a prescribed temperature profile (isothermal or non-isothermal). The framework of the model was described elaborately in [12] and is further extended here. A schematic representation of the model is shown in Figure 1. The evolution of a set of (spherical) grains that is representative for

the microstructure (hereafter referred to as representative grains), is predicted. For each grain, the evolution of the defect concentrations (in the form of dislocations, vacancies, self-interstitial atoms and their clusters) is predicted using Cluster Dynamics [?, 17]. The lattice damage that accumulates induces a bulk stored energy E^B in the microstructure, which is strongly temperature dependent and which may drive recrystallization. The nucleation of new, nearly defect-free grains and grain growth are described using a mean-field recrystallization model based on [18]. In this model, each representative grain interacts with surrounding averaged media (homogeneous equivalent media, HEMs). The amount of growth of grain k is determined by the differences in stored energy ΔE_k^{HEM} between each of the HEMs and the grain. As the grain boundaries move, the encountered defects are swept, so that grain growth affects both the defect concentrations and the grain radii. Two types of nucleation can occur in the model: bulk and necklace nucleation. The amount of nucleation that occurs at a certain time, depends on the nucleation activation barrier E_{act} (which depends on the amount of stored energy in the microstructure) and on the nucleation surface area A_{nuc} or nucleation volume V_{nuc} , available for necklace and bulk interaction, respectively. The grain boundary mobility m , which is strongly temperature dependent, plays an important role in the rates of grain growth and nucleation. The model is solved incrementally, in a staggered way, according to Figure 1.

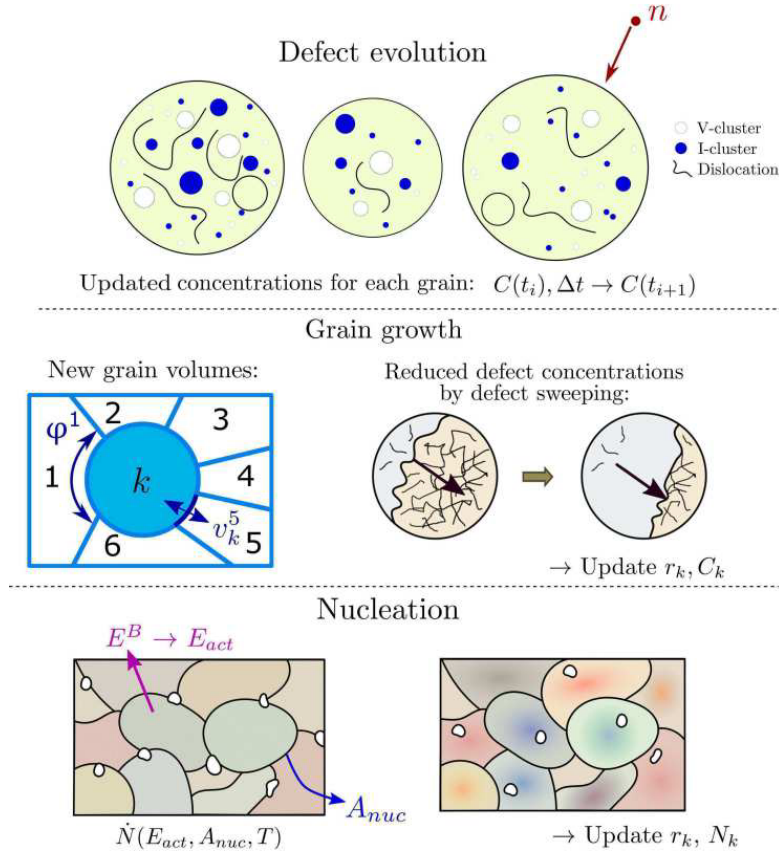


Figure 1: Schematic overview of the multi-scale model, showing the key mechanisms (defect evolution, grain growth and nucleation) and their impact on the microstructural evolution. Here, C is the defect concentration, $\Delta t = t_{i+1} - t_i$ is the size of the i^{th} time increment, ϕ^1 is the grain boundary surface fraction that is shared between HEM 1 and each representative grain k , v_k^5 is the velocity of the grain boundary segment that is shared between HEM 5 and grain k , r_k is the radius of grain k , C_k is the concentration of a defect in grain k , E^B is the bulk stored energy density, E_{act} is the activation energy for nucleation, A_{nuc} is the nucleation surface area, \dot{N} is the nucleation rate, T is the temperature and N_k is the number of grains that is represented by grain k .

2.2 Cluster dynamics

Neutron-induced displacement cascades result in the formation of many vacancies (V), self-interstitial atoms (I) and clusters of these (V_n , I_n , where n refers to the amount of vacancies or self-interstitial atoms contained in a cluster). Indirectly, the displacement cascades affect the dislocation density (ρ) as well: by climb and by Bardeen-Herring sources [19]. The evolution of the concentrations of the defect clusters is described by a set of coupled rate equations [17, ?], that consist of production (G), reaction (J) and annihilation (L) terms:

$$\frac{d}{dt} \left[C_{I_n} \right] = G_{I_n} + J_{n-1,n}^I + J_{n+1,n}^I - [J_{n,n-1}^I + J_{n,n+1}^I] - L_{I_n} C_{I_n}, \quad (1)$$

$$\frac{d}{dt} \left[C_{V_n} \right] = G_{V_n} + J_{n-1,n}^V + J_{n+1,n}^V - [J_{n,n-1}^V + J_{n,n+1}^V] - L_{V_n} C_{V_n}, \quad (2)$$

$$\frac{d}{dt} \left[\rho \right] = 2\pi v_{cl} S_{BH} - \rho \tau_{cl}^{-1}. \quad (3)$$

Here, C_{I_n} , C_{V_n} and ρ are the concentrations of self-interstitial clusters I_n , vacancy clusters V_n and the density of dislocations, respectively, and L represents the dislocation and grain boundary sinks for the mobile defects. $J_{n,n+1}^I$ represents the rate of the reactions $I_n + I \rightarrow I_{n+1}$ and $I_n \rightarrow I_{n+1} + V$ and analogous for the other J . Large I_n -clusters can become part of the dislocation network and the fraction of the growing clusters of size n that does that is denoted by f_n [20]. Dislocations can be generated by Bardeen-Herring sources and they can be removed by dipole annihilation. v_{cl} denotes the climb velocity, S_{BH} the density of Bardeen-Herring sources, and τ_{cl} the average dislocation lifetime prior to dipole annihilation. In the model, I_1 and V_1 are considered mobile. These are the defects that make absorption, emission and annihilation at sinks possible. The detailed expressions are given in Table 7 in Appendix A.

Note that the cluster dynamics model has a temperature-dependence and a grain size dependence. The temperature dependence can affect the absorption and emission rates (which depend on the diffusion of the mobile defects) and the climb velocity of the dislocations. The grain boundary sink strength depends on the grain size: in larger grains, the mobile defects have more difficulty to reach the grain boundaries. However, depending on the temperature, the smaller grains may be the fastest to accumulate damage, as the evolution of the defect concentrations are all interconnected.

Damage production

The temperature-dependent power law for the defect generation rates during displacement cascades was discussed before in [11, 12]. In this work, the expression is further refined to:

$$G_{\epsilon_n} = \frac{(1 - f_D/f_{max})\eta A_\epsilon}{n^{S_\epsilon}}. \quad (4)$$

Here, $\epsilon = I$ or V denotes the defect type, G_{ϵ_n} is the damage production rate of defects of size n and type ϵ , S_ϵ and A_ϵ are temperature-dependent parameters, with $A_\epsilon = G_0 / \sum_{n=1}^{N_{max}} n^{1-S_\epsilon}$. For intermediate temperatures, the parameter values are interpolated using the values of Table 1, which are based on MD-simulation results. Further, η is a parameter that denotes the fraction of defects, out of those that have survived the MD-simulations, that remain on longer time scales [12]. In this work, $\eta = 1$ is used, but similar simulations results (at different time scales) may be expected if a value of $\eta = 0.01$ would be used, based on limited simulations. Finally, the term $(1 - f_D/f_{max})$ ensures a decrease in defect production rate as damage accumulates in the material, where f_D denotes the atomic defect fraction, and f_{max} denotes the saturated defect fraction level.

Few studies are available regarding the defect saturation level in bcc metals. In 1996, Gao and Bacon studied the effect of overlapping cascades on the microstructural evolution for bcc-Fe, using MD-simulations [22]. Recently, Sand *et al.* [23] showed that the microstructural evolution due to overlapping cascades strongly differs from metal to metal. For the bcc metals Fe and W, subcascades easily form in Fe, while W displays compact cascades and cascade overlap is not required to form large defects. Here, only an educated guess of the defect saturation level can

T (K)	G_0 (# defects/atom s)	S_I	S_V
300	4.3×10^{-8}	2.20	1.63
1025	3.3×10^{-8}	2.50	1.86
2050	3.1×10^{-8}	2.17	2.42

Table 1: Parameter values for the defect production rate G_0 and power law exponents S_I and S_V at different temperatures, from [11], based on MD-results [21].

be made. To estimate this level, as a consequence of displacement cascades, it is assumed that during the thermal spike that accompanies the cascade, within the region where the melting temperature is exceeded, the pre-existing displacement defects are erased. Gao and Bacon found that the radius of the molten zone R_{melt} is related to the cascade energy E_p by $R_{melt} \approx 3a_0 E_p^{1/3}$, based on MD-results [22]. Furthermore, using the NRT-model [24], the amount of Frenkel pairs N_F created during the same cascade of energy E_p is approximately given by $N_F = 0.4 \frac{E_p}{E_d}$, where $E_d = 128$ eV is the displacement threshold energy for tungsten [21]. Assuming a spherically shaped thermal spike, this gives $f_{max} \approx N_F/N_{melt} = 0.01$, where N_{melt} is the number of atoms in the region that exceeds the melting temperature during the thermal spike. This is in the same range as the saturated defect fraction of 0.004-0.008 that was recently reported in [25], based on fcc studies. A lower bound for $f_{max} = 0.004$ is estimated based on the reported defect densities for neutron-irradiated tungsten in the fast neutron reactor JOYO at irradiation temperatures of 400-756 °C [26, 27]. In this work, the estimated value of $f_{max} = 0.01$ will be used in the simulations.

2.3 Mean-field recrystallization model

The original multi-scale model [12] consists of only two homogeneous equivalent media (HEMs), following [18]. It is extended to comprise more than two HEMs, which enables an improved description of the grain growth behaviour. The microstructure consists of representative grains, which are considered spherical with properties: radius r , a number of grains N that they represent, defect concentrations C and dislocation density ρ . As illustrated in Figure 2, each representative grain interacts with all the HEMs and each of those interactions results in the movement of a grain boundary segment. Together, the motion of the segments determines the amount of grain growth or shrinkage that occurs for a representative grain. The representative grains are

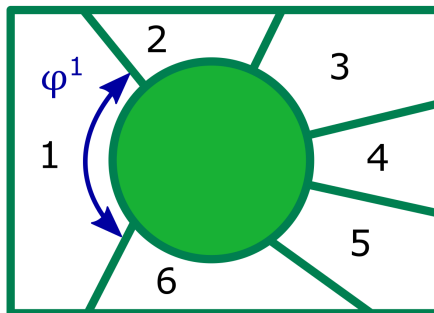


Figure 2: A representative grain, surrounded by 6 HEMs. The grain boundary surface fractions of the HEMs are denoted by ϕ .

assigned to a specific HEM based on their bulk stored energy densities, where for a number of HEMs N_{HEM} , there are $N_{HEM} - 1$ energy limits; e.g. all grains for which 10^5 J/m³ $\leq E^B < 10^6$ J/m³ could be in HEM 2, all representative grains for which 10^6 J/m³ $\leq E^B < 2.5 \times 10^6$ J/m³ in HEM 3, and so on.

Grain growth

Assuming that the grain boundary mobility m is constant throughout the microstructure, the amount of grain growth depends on the stored energy difference ΔE between two neighbouring

grains. The stored energy density E_k of a spherical representative grain k consists of a bulk contribution E_k^B and a surface contribution E_k^S and is given by

$$E_k = E_k^B + E_k^S = \sum_{n=1}^{N_{max}} \left[C_{I_n,k} E_{I_n}^f + C_{V_n,k} E_{V_n}^f \right] + \mu b^2 \rho_k / 2 - T S_k + 3\gamma_b / 2r_k, \quad (5)$$

where $C_{I_n,k}$ is the concentration of interstitial clusters of size n in grain k , $E_{I_n}^f$ is the formation energy for cluster I_n , and likewise for the vacancy clusters, μ is the shear modulus, b is the magnitude of the Burgers vector, ρ_k the dislocation network density in grain k , S_k is the configurational (mixing) entropy, γ_b the grain boundary energy and r_k the radius of grain k . The adopted parameter values [17, 19, 13] can be found in Table 7.

In the mean-field model, grain growth is calculated based on the stored energy difference between a grain and the HEMs, $\Delta E = E_q^{HEM} - E_k$. Here, E_q^{HEM} is the volume average of the stored energy density of all the grains that are contained in HEM q :

$$E_q^{HEM} = \frac{\sum_{k \in q} r_k^3 N_k E_k}{\sum_{\forall k} r_k^3 N_k}. \quad (6)$$

The volume change of a grain k that occurs in a time step $\Delta t = t_{i+1} - t_i$ is then given by:

$$\Delta V_k = \sum_{q=1}^{N_{HEM}} \Delta V_k^q = \sum_{q=1}^{N_{HEM}} \phi^q 4\pi r_k^2 v_k^q \Delta t = \sum_{q=1}^{N_{HEM}} \phi^q 4\pi r_k^2 m (E_q^{HEM} - E_k) \Delta t, \quad (7)$$

where ΔV_k^q is the volume change of grain k due to its interaction with HEM q , N_{HEM} is the number of HEMs, ϕ^q is the fraction of the grain boundary surface area of a grain that is shared with HEM q , v_k^q is the grain boundary velocity between HEM q and grain k , m is the grain boundary mobility. The grain boundary surface fraction that HEM q shares with any representative grain is

$$\phi^q = \frac{A_q}{A_{tot}} = \frac{\sum_{k \in q} N_k r_k^2}{\sum_{\forall k} N_k r_k^2}. \quad (8)$$

The grain boundary mobility is taken to be [11, 28]:

$$m(T) = K_m \frac{\beta \delta V_m}{b^2 RT} D_0^{GB} \exp\left(\frac{-Q^{GB}}{k_B T}\right), \quad (9)$$

where K_m is characterized based on static recrystallization experiments on tungsten ([13]), Q^{GB} is the activation energy for diffusion of tungsten along grain boundaries, δ is the thickness of the grain boundaries, $\beta=0.3$ is a fraction parameter [28], V_m is the molar volume, R is the gas constant and D_0^{GB} is the self-diffusivity of tungsten along the grain boundaries. The parameters are specified in Table 7 in Appendix A.

In the model it is assumed that the moving grain boundaries sweep the defects they encounter. Therefore, defect-free volume is added to growing grains, which leads to a reduction in the average defect concentrations in the grain [18, 12]. The solution procedure for grain growth in this multi-HEM mean-field approach is detailed in Appendix B, where it is also explained how the grains are assigned to the HEMs, how the total amount of representative grains is bounded and how volume conservation is satisfied.

Nucleation

Nucleation of new, defect-free, grains, is in principle expected to take place primarily at the grain boundaries for tungsten (necklace-type nucleation) [12, 13]. On top of that, under irradiation conditions, the displacement cascades may lead to a high lattice stored energy at the grain interior, which may trigger an additional nucleation mechanism: bulk nucleation. Both types of nucleation are illustrated in Figure 1. During nucleation, a small defected volume is replaced

by a defect-free volume and new grain boundary surface area emerges. The process is driven by the reduction in the Gibbs free energy ΔE , which is given by

$$\Delta E^S = \frac{1}{K_a^S} \left[-\frac{4\pi r^3}{3} (E^B - E_0^B) + 3\pi r^2 \gamma_b \right], \quad (10)$$

$$\Delta E^B = \frac{1}{K_a^B} \left[-\frac{4\pi r^3}{3} (E^{B,HD} - E_0^B) + 4\pi r^2 \gamma_b \right], \quad (11)$$

for necklace and bulk nucleation respectively. Here, r is the radius of the nucleus (new grain), $E^B = \sum_{q=1}^{N_{HEM}} \phi^q E^q$ is the average bulk stored energy density, E_0^B is the bulk stored energy density for a grain with equilibrium defect concentrations, $E^{B,HD}$ is the average bulk energy density for all the grains with a (HD, high) bulk energy density that exceeds the nucleation threshold ($E_k^B > E_{nuc}^{B,thr}$) and K_a^S and K_a^B are parameters for reduced activation energy during necklace and bulk nucleation respectively. A nucleation threshold applies, because nucleation is considered not to be possible at/in grains with a low defect density. Therefore, these low-defect density grains should not contribute to the average bulk stored energy, since this would lead to a higher nucleation activation barrier otherwise.

The necklace and bulk nucleation rates \dot{N}^S and \dot{N}^B are given by:

$$\dot{N}^S = K_N^S A_{nuc} \exp\left(\frac{-E_{act}^S}{k_B T}\right) \exp\left(\frac{-Q^{GB}}{k_B T}\right), \quad (12)$$

$$\dot{N}^B = K_N^B V_{nuc} \exp\left(\frac{-E_{act}^B}{k_B T}\right) \exp\left(\frac{-Q^{GB}}{k_B T}\right). \quad (13)$$

The nucleation rates depend on the nucleation activation energies E_{act}^S and E_{act}^B , the temperature T , the nucleation surface area A_{nuc} , the nucleation volume V_{nuc} , the activation energy for the grain boundary mobility Q^{GB} and the nucleation rate constants K_N^S and K_N^B . Necklace nucleation takes place at all grain boundary segments, except for the segments where both the representative grain and the HEM have bulk energies below the nucleation threshold ($E_{nuc}^{B,thr}$). This leads to the following expression for the nucleation surface area:

$$A_{nuc} = 2\pi \sum_i r_i^2 N_i \left[1 - \left(\frac{\sum_{j: E_j < E_{nuc}^{B,thr}} N_j r_j^2}{\sum_j N_j r_j^2} \right)^2 \right], \quad (14)$$

In this expression, the summations hold over all representative grains in the microstructure, unless specified otherwise. The nucleation volume V_{nuc} for bulk nucleation consists of the volume of all the grains for which $E^B > E_{nuc}^{B,thr}$. Stable nuclei will form when $\frac{\partial \Delta E}{\partial t} < 0$ and when $v_{GB}^{nuc} > 0$ (i.e. the nucleus is growing). Solving for these conditions gives the nucleation activation energies E_{act}^S and E_{act}^B and the nucleation radii r_{nuc}^S and r_{nuc}^B , as detailed in Appendix B.

HD daughter grains

Grains that form by bulk nucleation are called HD daughter grains (HD = high defect density), and all the other grains are referred to as regular grains. The HD-daughter grains only grow with respect to the representative grains for which $E^B > E_{nuc}^{B,thr}$. HD-daughter grains are converted to regular grains as soon as their radius exceeds $r^{HD}/4$, where r^{HD} is the average radius of all the grains for which $E^B > E_{nuc}^{B,thr}$, or when the bulk energy density of the HD-daughter grains exceeds $E_{nuc}^{B,thr}$ (see [12]).

2.4 Hardening

The displacement defects in the lattice induce hardening of the material, as they form obstacles for dislocation motion. A hardness indicator \mathcal{I}_H , based on the Dispersed Barrier Hardening model, is used to qualitatively study the evolution of the hardness under irradiation [2, 12]:

$$\mathcal{I}_H = \frac{\sqrt{\rho} + \frac{M}{\alpha_T} \sqrt{\sum_j 2\alpha_j^2 C_j r_j}}{\sqrt{\rho_0}}. \quad (15)$$

Here, M is the Taylor factor, α_T is the dislocation barrier strength, ρ_0 is the initial dislocation density, α_n is the defect barrier strength of defect type n (see Table 2) and r_n is the radius of defect type n , see Equations 27 and 28 in Appendix A.1.

	Barrier strength factor α	Diameter (nm)	Cluster size N
Interstitial loop	0.15	1.0-2.7	14-100
Void	0.25	1.0-1.4	33-100

Table 2: Barrier strengths as used in the DBH-model, based on [2], for the cluster sizes as listed. For clusters of smaller sizes, $\alpha = 0$ is taken.

2.5 Parameter characterization

The parameters K_m , K_N and K_a , that are related to the grain boundary mobility, the nucleation rate and the reduced nucleation activation energy, have been identified by performing static recrystallization simulations using the mean-field recrystallization model and the experimental results of Lopez *et al.* [13]. Reparameterization (with respect to [11]) is performed here because in the improved model, the surface fractions are calculated differently. Only necklace nucleation is assumed to take place here, based on experimental observations of static recrystallization of tungsten [13]. The initial and final microstructural parameters are listed in Table 3. The original microstructure consisted of 500 representative grains with normally distributed sizes and dislocation densities. 2 HEMs were used, with the bulk energy threshold for the second HEM taken as 10^6 J/m³ and with a nucleation energy density threshold of $E_{nuc}^{B,thr} = 10^6$ J/m³. The

Property	Value	Source
<i>Initial microstructure</i>		
Initial average grain size \bar{r}_i	18.6 μm	[13]
Standard deviation for \bar{r}_i	3.1 μm	
Initial average dislocation density $\bar{\rho}_i$	$3.2 \times 10^{14} \text{ m}^{-2}$	[13]
Standard deviation for $\bar{\rho}_i$	$5.2 \times 10^{13} \text{ m}^{-2}$	
<i>Final microstructure</i>		
Final average grain size \bar{r}_f (after 25 hr at $T=1200$ °C)	54.1 μm	[13]
Final dislocation density ρ_f	$1 \times 10^9 \text{ m}^{-2}$	[17]

Table 3: Initial and final microstructural properties, before and after static recrystallization, based on [13].

obtained fit (for $K_a^S = 5 \times 10^7$, $K_m = 1490$ and $K_N^S = 2.5 \times 10^{17} \text{ m}^{-2} \text{ s}^{-1}$) is shown in Figure 3a and is in adequate agreement with the experimental data. Initially, the parameter identification was done for $T=1200$ °C; once a satisfactory fit for this temperature was found, the temperature dependence was also taken into the consideration. Parameters K_a^S and K_m and K_N^S were determined such that full recrystallization would be obtained after 25 hours, with a final grain size of 54.1 μm . It was found that given K_a^S , a unique set of K_m and K_N^S exists that fullfills these requirements, as illustrated in Appendix C. Figure 3b shows the temperature dependence of the time required to reach a recrystallized volume fraction $f^{RX}=0.50$, both for the experimental results and for the simulation results, expressed by the slope $a = \Delta \log_{10}(t_{1/2})/\Delta T$ of the recrystallization time as a function of temperature. The slope was determined for various choices of K_a^S (with the corresponding K_m and K_N^S such that the expected final grain size and expected recrystallization time is reached at 1200 °C). It was found that the slope a depends on the parameter K_a^S , as shown in Figure 3c. This dependence converges to a plateau and it is not possible to choose K_a^S such that the experimental slope is recovered. Below, the influence of the choice of K_a^S on the microstructural evolution under neutron irradiation will be shown. For each of the choices for K_a^S (with the corresponding K_m and K_N^S), the shape of the evolution of the recrystallized volume fraction f^{RX} under static recrystallization is the same (not shown).

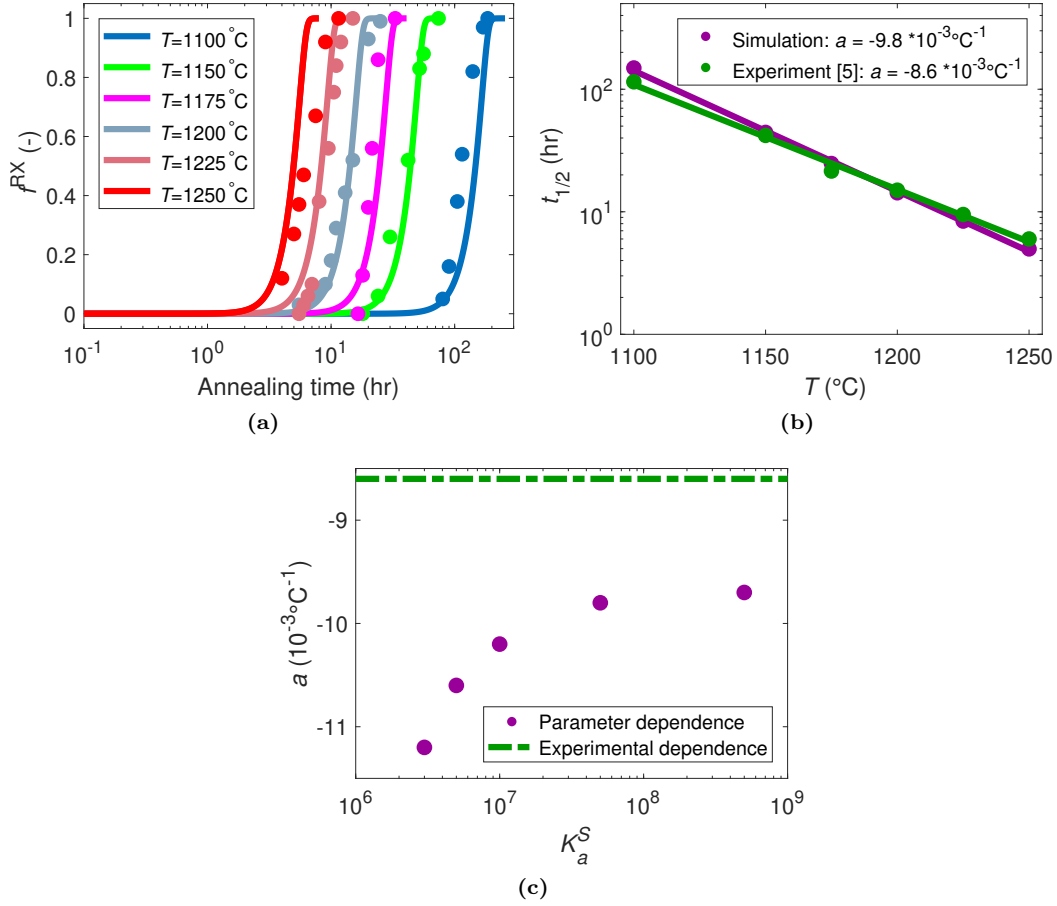


Figure 3: (a) Simulation results for the evolution of the recrystallized volume fraction f^{RX} as a function of annealing time during static recrystallization, for various temperatures, compared to experimental results obtained by Lopez [13], from hardness measurements and EBSD, for warm-rolled samples that were thickness-reduced with 90%. (b) Temperature-dependence of the half-time for recrystallization, including a fit of the slope, for the experimental results and for the simulations; (c) Influence of K_a^S on the temperature-dependence of the speed of recrystallization, slope a .

However, there is another difference: a lower value for K_a is accompanied by a higher value of K_N^S and a nucleation rate that is initially higher and decreases afterwards, while a high value for K_a^S leads to lower nucleation barrier and a nearly constant nucleation rate. The total amount of new grains over the course of the simulation is the same for both cases. The final grain size distribution will be slightly broader in the case of a high value for K_a^S , because of the constant nucleation rate, that leads to more heterogeneous sizes for the new grains.

K_a^S	K_N^S ($\text{m}^{-2}\text{s}^{-1}$)	K_m	K_{m_0}	Previous/current
3×10^6	9.3×10^{26}	1335	-	Current
5×10^7	2.5×10^{17}	1490	-	Current
1×10^8	3.16×10^{17}	1.8×10^4	25	Previous

Table 4: Two currently possible parameter sets identified from the experimental data and the previous parameter set, that includes a reduced grain boundary mobility for pinned grains, K_{m_0} .

Parameter effects on the full model

Based on the results shown in Figure 3, there is too little information to determine for which value of K_a^S the reality is best represented, other than that for a higher value of K_a^S , the temperature dependence is slightly better matched. In Figure 4a and b it is shown how much the results

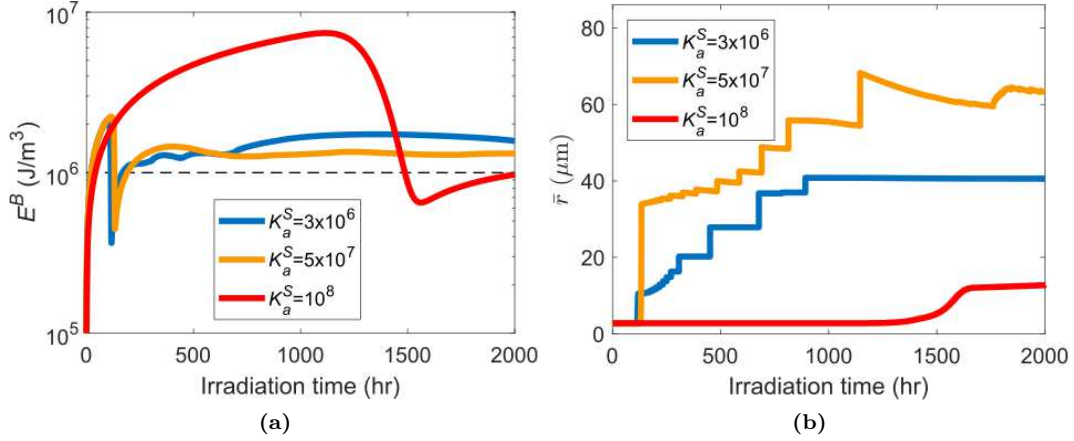


Figure 4: (a) Evolution of the bulk stored energy density E^B and of the (b) average grain size \bar{r} for different parameter sets during neutron irradiation at $T=1100$ °C. The dashed line shows the threshold that separates the two HEMs for the simulation with $K_a^S = 10^8$.

for the full model for neutron-induced recrystallization are affected by the set of recrystallization parameters. Simulations were performed using $K_a^S = 3 \times 10^6$ and $K_a^S = 5 \times 10^7$ (see Table 4) at $T=1100$ °C and are compared to the simulation results that were obtained with $K_a^S = 1 \times 10^8$ (see Table 4), using the previous method for calculating the surface fractions and using only 2 HEMs. For the present simulations 20 HEMs were used, with 50 representative grains in each HEM. From Figure 4a and b it becomes clear that the recrystallization parameters clearly affect the evolution of the mean grain size, whereas the bulk stored energy evolves similarly for either of the two recrystallization parameter sets. These results show that in spite of the fact that the values for the nucleation parameters are uncertain, the multi-scale model is not very sensitive to the choice of these parameters. To obtain more accurate recrystallization parameters, the model could be parameterized better with experimental data that entail the final grain size and half-time $t_{1/2}$ of recrystallization for several temperatures. Additional information about the evolution of the grain size distribution would improve the parameterization as well.

The experimentally determined temperature-dependency of the recrystallization half-time, captured with slope a , is uncertain for several reasons: (1) at high annealing temperatures, when the recrystallization half-time is small, the effect of the ramp time to heat the sample may be non-negligible; (2) for most temperatures, the recrystallized fraction was only determined from hardness measurements, whereas EBSD-data would be more reliable and (3) the information on the initial and final grain size is not very precise. Nevertheless, to capture the current experimental temperature-dependency of the recrystallization half-times correctly, further extensions of the mean-field model for recrystallization would be needed. For example, it may then be necessary to include the effect of the grain shapes and/or grain orientations on the grain boundary mobility.

In the remainder of this article, the parameter set with $K_a=5 \times 10^7$ will be used.

3 Results

3.1 Isothermal microstructural evolution

Figure 5 shows the microstructural evolution, as expressed by the bulk energy density E^B , the average grain size \bar{r} , the hardness indicator \mathcal{I}_H and the volume fraction of original grains during irradiation at temperatures of 800°C, 900°C and 1000°C, considering necklace nucleation only. The simulation settings for the representative grains and the HEMs can be found in Appendix A. Note that E^B is defined as the summation of the energies of the HEMs, weighted with their respective surface fractions, while for \mathcal{I}_H , the overall volume averaged concentrations are used.

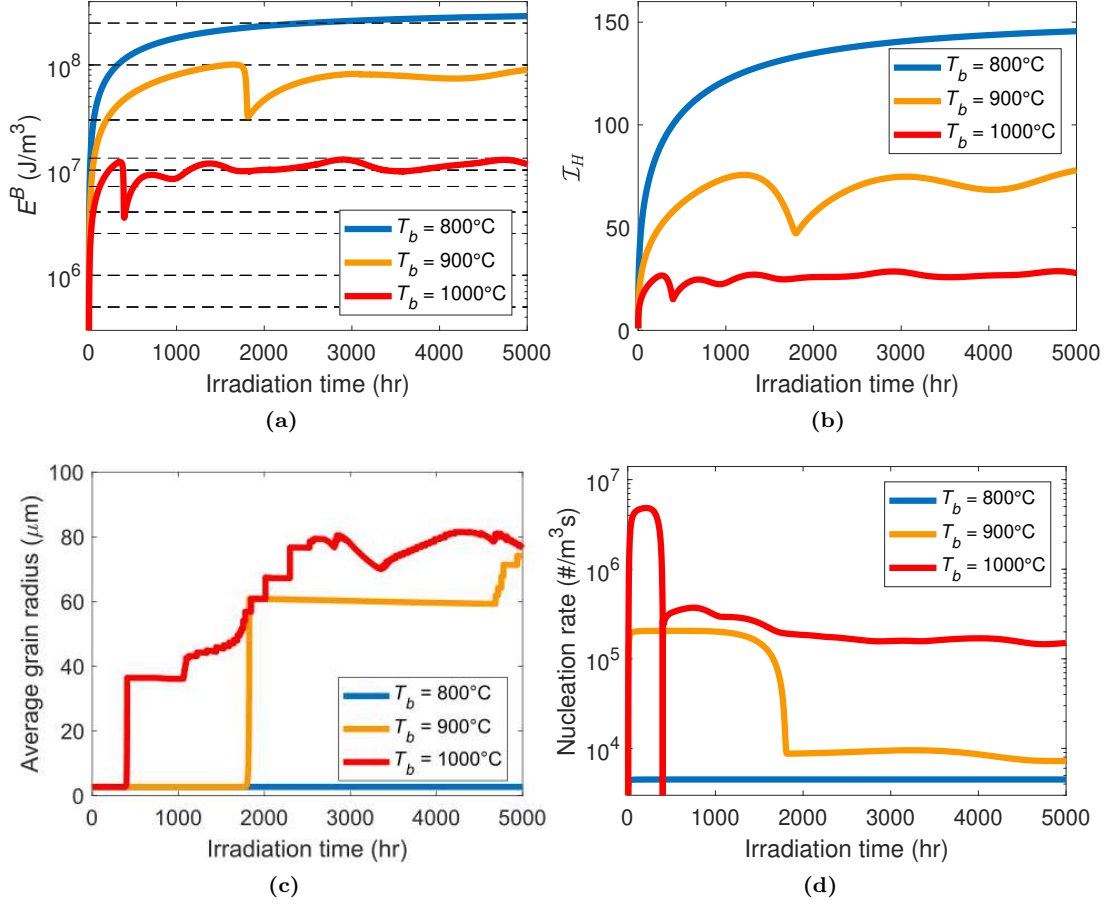


Figure 5: Temporal evolution of (a) the bulk stored energy density E^B , (b) the hardness indicator I_H , (c) the average grain radius \bar{r} and (d) the nucleation rate, during irradiation at temperatures 800 °C, 900 °C and 1000 °C. The dashed lines in (a) indicate the energy limits of the HEMs.

For the adopted nucleation parameters, recrystallization takes place rapidly at an irradiation temperature of 1000 °C. The hardness indicator stays under the value of 30. For 900 °C, recrystallization only sets in after more than 1000 hours of irradiation with a maximum value for the hardness indicator of 80. For 800 °C, no recrystallization takes place in the first 4000 hrs and the hardness indicator approaches 150 and keeps increasing. Figure 5 reveals that cyclic recrystallization takes place for the temperatures of 900 °C and 1000 °C, indicating that the average grain size keeps increasing until it saturates (as a result of the balance between the nucleation rate, the amount of damage by irradiation and the amount of recovery by growth of the nucleated grains). A potential reduction of the high hardness found at 800 °C, using heat treatments, is thereby suggested. Therefore, 800 °C is selected as the base temperature for simulations of non-isothermal heat treatments.

3.2 Non-isothermal microstructural evolution

In the next simulations, it will be explored how much recovery can be obtained by heating repeatedly for a short amount of time. Figure 6a shows the typical temperature profile that is applied every 500 hrs (or every 100 hrs) in the next simulations. The material is heated in 10 min to the annealing temperature of 1200 °C, at which it is kept for 1 hr and after which the material is cooled back to 800 °C in 10 min. At first, only necklace nucleation is considered, and thereafter, the combination of necklace and bulk nucleation is considered.

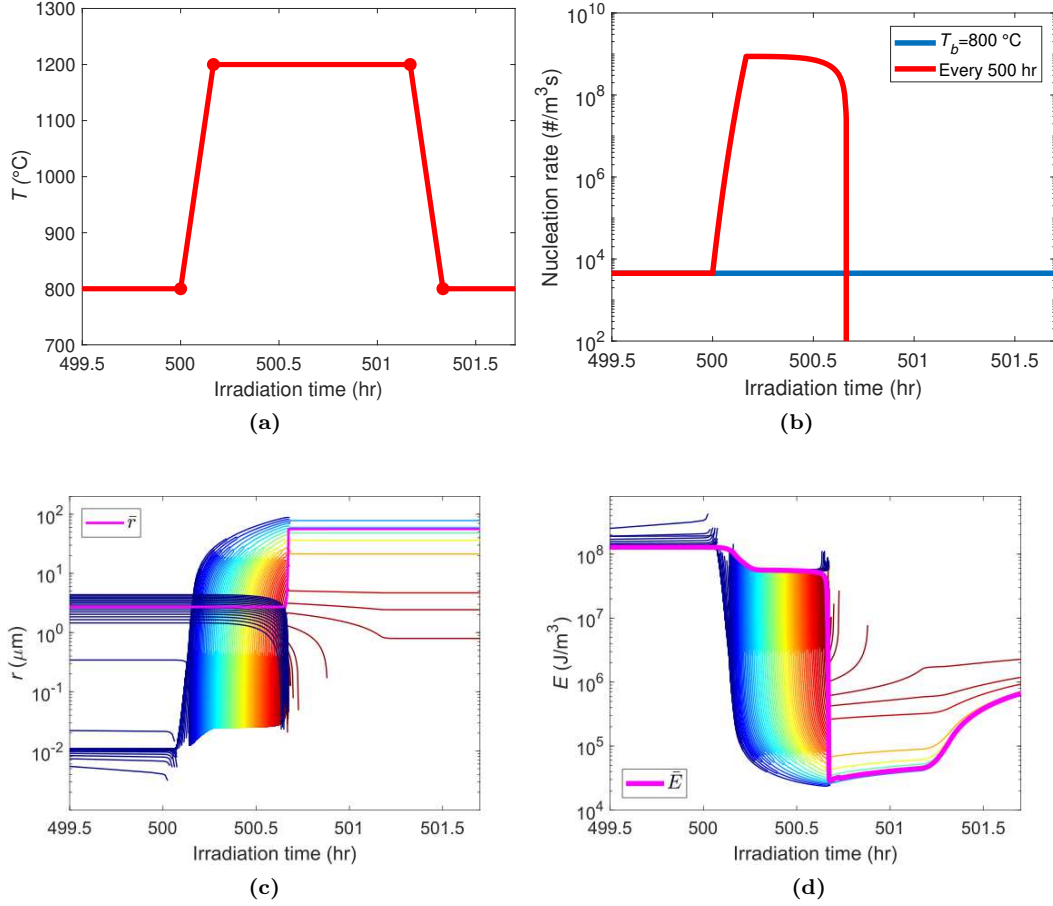


Figure 6: (a) Typical temperature profile during the applied heat treatment; (b)-(d) Microstructural evolution during heat treatment; (b) Nucleation rate (in comparison to the nucleation rate in the isothermal simulation at 800 °C); (c) Evolution of the grain radius and (d) evolution of the stored energy density of the representative grains. The colors in (c-d), from blue to red, indicate the order in which the new grains formed. Lines end when grains are completely consumed by other grains, or when grains merge with other representative grains, which occurs when the maximum amount of representative grains in a HEM is exceeded, see Appendix B.

Figures 6 b-d show the microstructural evolution that occurs during the first heat treatment cycle (annealing at 1200 °C) after 500 hrs of irradiation at 800°C: the nucleation rate rises (Figure 6b) because of the increased temperature, which affects the exponential terms in Equation 13. The increased grain boundary mobility and the high amount of new nuclei lead to a fast, complete recrystallization: the original representative grains shrink in size until they vanish (Figure 6c) and the stored energy density of the nucleated grains (Figure 6d) decreases, while they grow to become large grains. Upon full recrystallization, the average stored energy density (pink line) drops and the average grain radius increases, as shown in Figures 6c and d. Once the average stored energy density decreases, the nucleation rate also drops. The material is cooled down to 800 °C again, and up to 1000 hrs (when the next cycle of extra heating starts) the mobility of the grain boundaries and point defects again decreases, making recovery difficult, whereas the stored energy due to lattice damage will accumulate again.

The effects of repeated heating, every 100 hrs and every 500 hrs, are shown in Figure 7 and are compared to the isothermal irradiation situation.

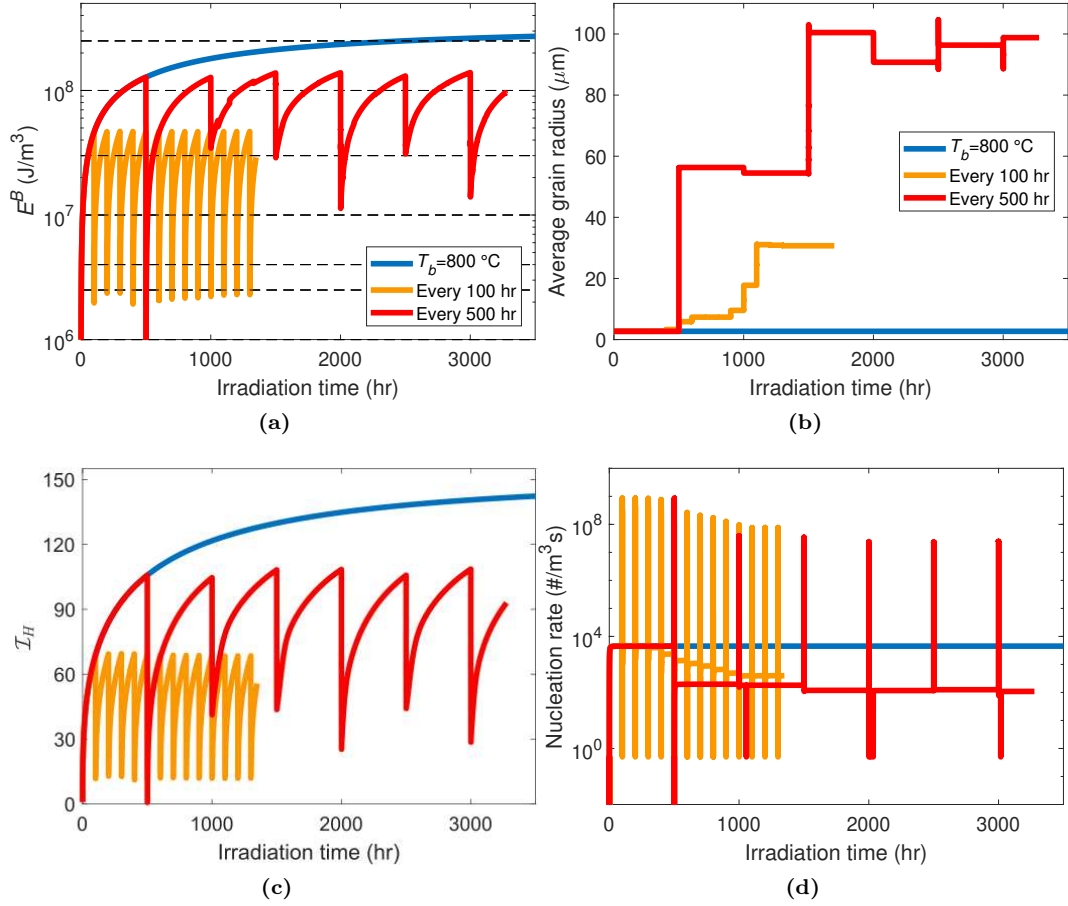


Figure 7: Temporal evolution of (a) the bulk stored energy density E^B , (b) the hardness indicator \mathcal{I}_H , (c) the average grain radius \bar{r} and (d) the nucleation rate, during irradiation, for repeated heat treatments every 100 hr, every 500 hr, in comparison to the evolution under isothermal conditions. The dashed lines in (a) indicate the energy limits of the HEMs.

In the isothermal situation, the hardness indicator reaches 140, see Figure 7c. By heating every 500 hrs for 1 hr to 1200 °C, its value can be limited to a value below 110 and by heating more frequently, every 100 hrs, it stays below 70. For the 500 hrs repetitive heat treatment, for the first cycle, full recrystallization takes place, where E^B drops by several orders of magnitude (Figure 7a). During the second cycle, the amount of grain boundary area per volume is smaller, as the average grain size is larger (Figure 7b). This leads to a lower nucleation rate (Figure 7d) and full recrystallization is no longer achieved (E^B does not drop below 5×10^7 J/m^3 at 1000 hrs). Nevertheless, \mathcal{I}_H reduces considerably and it does not seem to be critical to reach full recrystallization, as long as a sufficient amount of recovery is achieved. If the annealing is applied every 100 hrs, full recrystallization is not achieved during the first cycle, as the driving force for recrystallization is lower after 100 hrs of irradiation, which means that the full recrystallization process completes less easily within 1 hr of annealing at 1200 °C. The expected maximum increase of the hardness indicator for a certain interval of time between cyclic heat treatments is related to its evolution under isothermal conditions (Figure 7c): each new cycle following a heat treatment entails a hardness indicator that increases to the same level at the start of the first cycle. Yet, the peaks in \mathcal{I}_H can be slightly higher if the recrystallization was incomplete during the previous cycle.

Temperature of annealing In Figure 8a, the influence of the annealing temperature on the hardness indicator is shown, only considering necklace nucleation. An annealing temperature T_h of 1000 °C during 1 hr after every 100 hrs does not result in full recrystallization, but \mathcal{I}_H is somewhat reduced: during the first 1800 hrs, the maximum value is 113, compared to 138 for

the isothermal simulation at 800 °C. For higher annealing temperatures, of 1050 °C and 1100 °C, the maxima are 94 and 82, respectively (for the selected parameter set). For 1200 °C and 1400 °C, the maximum is the same, 74. Also, for the annealing temperature of 1000 °C, the maximum for the hardness indicator keeps increasing, whereas for the higher temperatures, the maximum remains stable.

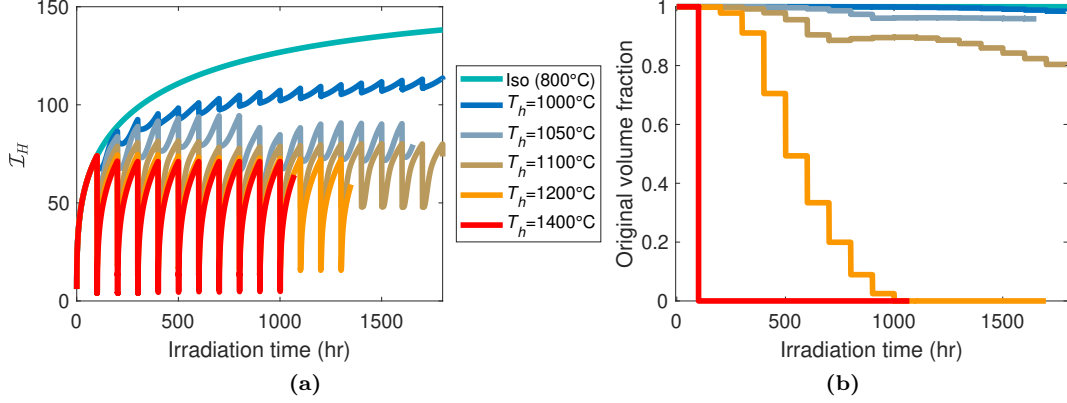


Figure 8: The effect of the annealing temperature T_h on (a) the evolution of the hardness indicator \mathcal{I}_H , during annealing every 100 hrs for 1 hr, and (b) the evolution of the original volume fraction.

Figure 8b displays the evolution of the original volume fraction, which clearly reveals the moment at which no original grains are left in the microstructure. For an annealing temperature of 1400 °C and higher, full recrystallization takes place during the first annealing cycle, while for 1200 °C, the original microstructure vanishes only in the 10th cycle. At 1100 °C or lower, even 18 cycles are not sufficient for full recrystallization to take place.

Bulk nucleation effects So far, only necklace nucleation has been considered, as parameterization of the model was done assuming necklace nucleation only. However, the average grain radius rises significantly after the first recrystallization, and bulk nucleation could have a significant effect on the obtained microstructure. Here, the effects for bulk nucleation with $K_N^B = 10^{24} \text{ m}^{-3}\text{s}^{-1}$ and for two values of K_a^B , $K_a^B=10^5$ and $K_a^B=10^6$, are shown in Figure 9.

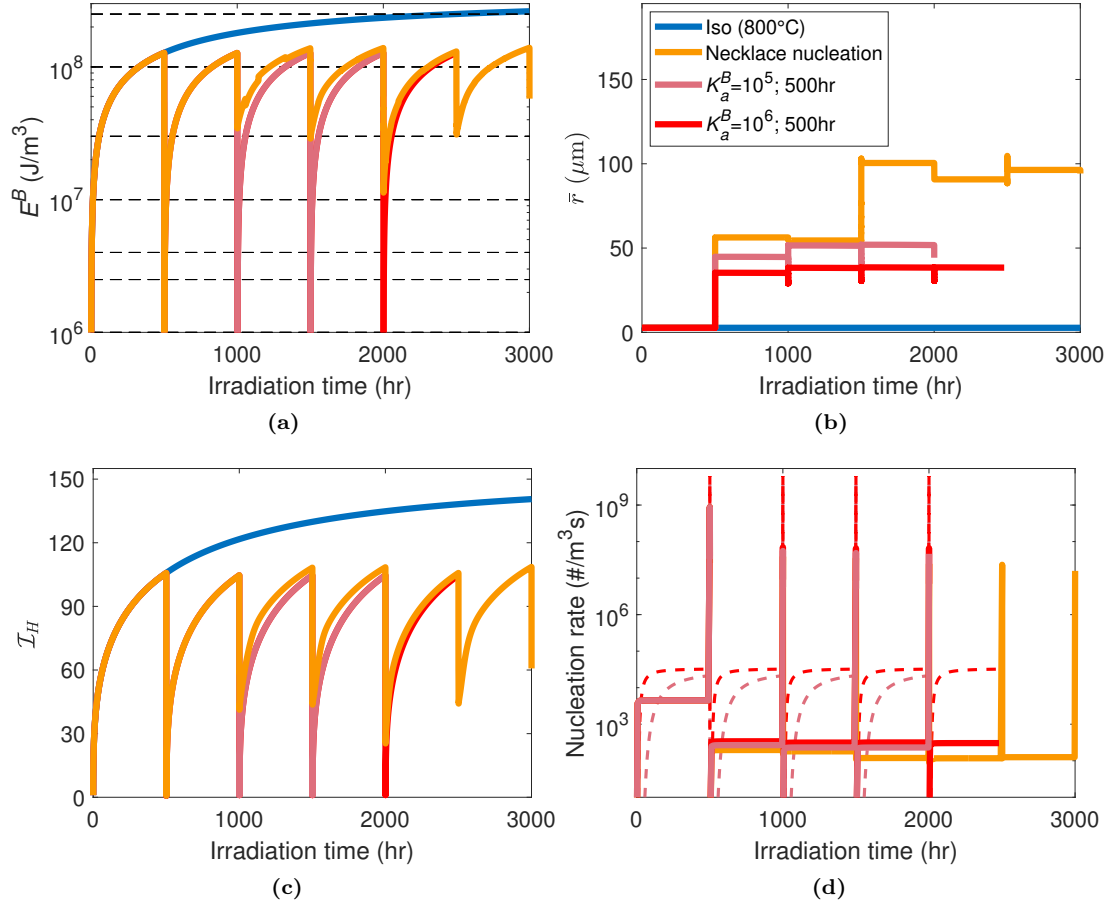


Figure 9: Temporal evolution of (a) the bulk stored energy density E^B , (b) the hardness indicator \mathcal{I}_H , (c) the average grain radius \bar{r} and (d) the bulk (dashed line) and necklace (solid line) nucleation rate, during irradiation at 800 °C, with repeated annealing at 1200 °C every 500 hrs, for different bulk nucleation parameters.

Bulk nucleation affects the average grain size significantly (Figure 9b), because of the higher nucleation rate, but the increase of the hardness indicator is only marginally affected by the extra nucleation mechanism (Figure 9c). The bulk nucleation rate mostly exceeds the necklace nucleation rate. As a general rule, as long as (nearly) full recrystallization is achieved during the annealing period, it does not matter for the hardness indicator how much nucleation takes place. This implies that the more bulk nucleation occurs, the lower the annealing temperature can be, while still achieving full recrystallization.

4 Conclusions

The divertor of the nuclear fusion reactors ITER (and DEMO), with plasma-facing parts made out of tungsten, will be heavily damaged during neutron displacement cascades, which leads to strong irradiation hardening, accompanied by a loss of ductility. At sufficiently high temperatures, neutron-induced recrystallization is expected to take place, which (partially) removes the irradiation hardening. At intermediately high temperatures, on the order of 800°C, recrystallization does not take place easily and interim annealing treatments inducing recrystallization may be an interesting option for regions in the monoblocks where this temperature is not exceeded.

In this work, it is explored whether the hardening of neutron-irradiated tungsten might be appreciably reduced by applying repeated cyclic heat treatments. Use is made of a multi-scale model for the microstructural evolution combined with a mean-field recrystallization model (with

multiple homogeneous equivalent media) and a cluster dynamics model for the neutron damage. Here, a base temperature of 800 °C was used, and the annealing heat treatments were applied every 100 hrs or every 500 hrs, during 1 hr at 1200 °C. The evolution of the hardness was studied qualitatively, using a hardness indicator, which is a function of the concentrations of irradiation defects. For the selected parameter set, it was found that with these treatments, the hardness indicator reduced significantly (here, from more than 140 to less than 70, by heating every 100 hrs, or to 110, by heating every 500 hrs). Increasing the frequency of the cyclic heating can further reduce the value of the hardness indicator.

The annealing temperature for the heat treatments was varied from 1000 °C to 1400 °C. It was found that the hardness indicator reduces significantly as long as the annealing temperature is chosen sufficiently high to achieve at least partial recrystallization (here, minimum 1050 °C, for heating every 100 hrs with a base temperature of 800 °C).

Under cascade damage conditions, the stored energy may be high in the grain interior, which possibly entails significant bulk nucleation, whereas for strain-induced recrystallization, nucleation mostly takes place near the grain boundaries. The simulation results show that under these circumstances, a higher total nucleation rate is expected during the heat treatments, leading to a faster or more progressed (partial) recrystallization. As a result, a lower annealing temperature might suffice in the case that bulk nucleation takes place.

A systematic parameter characterization of the model was carried out in this study, based on experimental data from static recrystallization experiments. The analysis shows the need for more experimental data, mostly to validate and better capture the temperature-dependency of the microstructural evolution during recrystallization. Furthermore, experimental information is lacking to make an optimal and unique choice for the parameters, which affects the prediction of the grain size evolution. Such experiments should provide temperature-dependent information on the initial and final (average) grain size, initial defect density, as well as on the evolution of the recrystallized fraction. More reliable information on the recrystallization behaviour may also lead to the need to refine the mean-field recrystallization model.

The evolution of the hardness indicator that was found here shows that the yield strength of tungsten may vary considerably when the reactor is in operation. Recrystallization might be a way to limit the (maximum) hardness and improve the ductility. Cyclic heat treatments are suggested as a possible route to improve the lifetime of the tungsten monoblocks. In order to apply such heat treatments, a change in the monoblock design might be needed, as the temperature of tungsten close to the cooling tube is now too limited by the maximum temperature of the cooling tube and the cooling fluid.

A Defect evolution details

The full set of cluster dynamics equations (that were summarized by Equation 1 and 2), which are adapted from [17] and [20], is given below. The largest vacancy cluster size is N_V and the largest interstitial cluster size is N_I .

A.1 The full Cluster Dynamics equations

$$\begin{aligned} \frac{dC_I}{dt} = & G_I + k_{I_2+V}^+ C_{I_2} C_V + 2\alpha_2^- C_{I_2} + \sum_{n=3}^{N_I} \alpha_n^- C_{I_n} - k_{I+V}^+ (C_I C_V - C_I^{eq} C_V^{eq}) \\ & - 2\alpha_1^+ C_I^2 - \sum_{n=2}^{N_I} \alpha_n^+ C_I C_{I_n} - \sum_{n=2}^{N_V} k_{V_n+I}^+ C_I C_{V_n} - (k_{D+I}^+ + k_{S+I}^+) C_I, \end{aligned}$$

$$\begin{aligned}
\frac{dC_{I_2}}{dt} &= G_{I_2} + \alpha_1^+ C_I^2 + k_{I_3+V}^+ C_{I_3} C_V + \alpha_3^- C_{I_3} + k_{I_2-V}^- C_I \\
&\quad - \alpha_2^- C_{I_2} - \alpha_2^+ C_{I_2} C_I - k_{I_2-V}^- C_{I_2} - k_{I_2+V}^+ C_{I_2} C_V, \\
\frac{dC_{I_n}}{dt} &= G_{I_n} + \alpha_{n+1}^- C_{I_{n+1}} + \alpha_{n-1}^+ C_I C_{I_{n-1}} + k_{I_{n-1}-V}^- C_{I_{n-1}} - \alpha_n^+ C_I C_{I_n} + k_{I_{n+1}+V}^+ C_V C_{I_{n+1}} \\
&\quad - \alpha_n^- C_{I_n} - k_{I_n+V}^+ C_V C_{I_n} - k_{I_n-V}^- C_{I_n}, \quad \text{for } 3 \leq n \leq N_I - 2, \\
\frac{dC_{I_{N_I-1}}}{dt} &= G_{I_{N_I-1}} + \alpha_{N_I}^- C_{I_{N_I}} + \alpha_{N_I-2}^+ C_I C_{I_{N_I-2}} + k_{I_{N_I-2}-V}^- C_{I_{N_I-2}} - \alpha_{N_I-1}^+ C_I C_{I_{N_I-1}} \\
&\quad - \alpha_{N_I-1}^- C_{I_{N_I-1}} - k_{I_{N_I-1}+V}^+ C_V C_{I_{N_I-1}} + k_{I_{N_I}+V}^+ C_V C_{I_{N_I}} - k_{I_{N_I-1}-V}^- C_{I_{N_I-1}}, \\
\frac{dC_{I_{N_I}}}{dt} &= G_{I_{N_I}} + \alpha_{N_I-1}^+ C_I C_{I_{N_I-1}} + k_{I_{N_I-1}-V}^- C_{I_{N_I-1}} - \alpha_{N_I}^- C_{I_{N_I}} - k_{I_{N_I}+V}^+ C_V C_{I_{N_I}}, \\
\frac{dC_V}{dt} &= G_V + 2\gamma_2^- C_{V_2} + k_{V_2+I}^+ C_{V_2} C_I + \sum_{n=3}^{N_V} \gamma_n^- C_{V_n} \\
&\quad + \sum_{n=2}^{N_I+1} k_{I_{n-1}-V}^- C_{I_{n-1}} - k_{I+V}^+ (C_I C_V - C_I^{eq} C_V^{eq}) - 2\gamma_1^+ C_V^2 \\
&\quad - \sum_{n=2}^{N_V} \gamma_n^+ C_V C_{V_n} - \sum_{n=2}^{N_I} k_{I_n+V}^+ C_V C_{I_n} - (k_{D+V}^+ + k_{S+V}^+) C_V, \\
\frac{dC_{V_n}}{dt} &= G_{V_n} + k_{V_{n+1}+I}^+ C_I C_{V_{n+1}} + \gamma_{n+1}^- C_{V_{n+1}} - k_{V_n+I}^+ C_I C_{V_n} + \gamma_{n-1}^+ C_V C_{V_{n-1}} - \gamma_n^- C_{V_n} \\
&\quad - \gamma_n^+ C_V C_{V_n}, \quad \text{for } 2 \leq n \leq N_V - 2, \\
\frac{dC_{V_{N_V-1}}}{dt} &= G_{N_{N_V-1}} + k_{V_{N_V}+I}^+ C_I C_{V_{N_V}} + \gamma_{N_V}^- C_{V_{N_V}} + \gamma_{N_V-2}^+ C_V C_{V_{N_V-2}} \\
&\quad - k_{V_{N_V-1}+I}^+ C_I C_{V_{N_V-1}} - \gamma_{N_V-1}^- C_{V_{N_V-1}} - \gamma_{N_V-1}^+ C_V C_{V_{N_V-1}}, \\
\frac{dC_{V_{N_V}}}{dt} &= G_{N_{N_V}} + \gamma_{N_V-1}^+ C_V C_{V_{N_V-1}} - k_{V_{N_V}+I}^+ C_I C_{V_{N_V}} - \gamma_{N_V}^- C_{V_{N_V}}.
\end{aligned}$$

The formulas for computation of each rate coefficient can be found in Table 5, and the calculation of several parameters in this table is specified hereafter. The parameter values that have been used can be found in Table 7. The expressions related to the evolution of the dislocation density are detailed in section A.2.

Dislocation loop I_n		
<i>Absorption rate</i>	<i>Emission rate</i>	
$\alpha_n^+ = 2\pi r_{I_n} Z_{I_n}^I D_I$	$\alpha_n^- = 2\pi r_{I_{n-1}} Z_{I_{n-1}}^I D_I \exp(-E_{I_n-I}^b/k_B T)/V_{at}$	Interstitial
$k_{I_n+V}^+ = 2\pi r_{I_n} Z_{I_n}^V D_V$	$k_{I_{n-1}-V}^- = 2\pi r_{I_{n-1}} Z_{I_{n-1}}^V D_V \exp(-E_{I_n-V}^b/k_B T)/V_{at}$	Vacancy
$k_{I+V}^+ = 4\pi r_{IV} (D_I + D_V)$	-	VI-recombination
Vacancy cluster V_n		
<i>Absorption rate</i>	<i>Emission rate</i>	
$k_{V_n+I}^+ = 4\pi r_{V_n} D_I$	-	Interstitial
$\gamma_n^+ = 4\pi r_{V_n} D_V$	$\gamma_n^- = 4\pi r_{V_{n-1}} D_V \exp(-E_{V_n-V}^b/k_B T)/V_{at}$	Vacancy

Table 5: Rate coefficients. The superscript ‘+’ denotes absorption of a point defect and the subscript ‘-’ denotes emission.

The sink strength sums of Table 6 are given by:

$$\left(S_I^{sk}\right)^2 = \frac{1}{D_I} \left[\sum_{n=1}^{N_I-1} \alpha_n^+ C_{I_n} + \sum_{n=1}^{N_V} k_{V_n+I}^+ C_{V_n} \right] + \rho Z_D^I, \quad (16)$$

$$\left(S_V^{sk}\right)^2 = \frac{1}{D_V} \left[\sum_{n=1}^{N_V-1} \gamma_n^+ C_{V_n} + \sum_{n=1}^{N_I} k_{I_n+V}^+ C_{I_n} \right] + \rho Z_D^V. \quad (17)$$

Dislocation sink ρ_D	
$k_{D+I}^+ = \rho Z_D^I D_I$	Interstitial
$k_{D+V}^+ = \rho Z_D^V D_V$	Vacancy
Grain boundary sink	
$k_{S+I}^+ = 3S_I^{sk} D_I / r_{grain}$	Interstitial
$k_{S+V}^+ = 3S_V^{sk} D_V / r_{grain}$	Vacancy

Table 6: Rate coefficients related to the strengths of the sinks (grain boundaries and dislocations).

The binding energies, that are used in the expressions for the emission rates are calculated using the capillarity approximation, using [17]:

$$E_{I_n}^f = E_{I_{n-1}}^f + E_I^f - E_{I_{n-1}}^b \text{ (by definition),} \quad (18)$$

$$E_{I_{n-1}}^b = E_I^f + \frac{E_{I_2}^b - E_I^f}{2^{2/3} - 1} [n^{2/3} - (n-1)^{2/3}], \quad (19)$$

$$E_{I_{n-1}}^b = E_V^f + \frac{E_I^f - E_{I_2}^b}{2^{2/3} - 1} [n^{2/3} - (n-1)^{2/3}], \quad (20)$$

$$E_{V_{n-1}}^b = E_V^f + \frac{E_{V_2}^b - E_V^f}{2^{2/3} - 1} [n^{2/3} - (n-1)^{2/3}]. \quad (21)$$

The diffusion coefficients of the isolated point defects I and V are given by:

$$D_I = D_{I_0} \exp(-E_I^m / k_B T), \quad (22)$$

$$D_V = D_{V_0} \exp(-E_V^m / k_B T). \quad (23)$$

The dislocation bias factors, used in the dislocation network sink rate and the absorption rates for vacancies and self-interstitial atoms by self-interstitial defect clusters are:

$$Z_{I_n}^I = Z_D^I \max\left[\frac{2\pi}{\ln(8r_{I_n}/r_p)}, 1\right], \quad (24)$$

$$Z_{I_n}^V = Z_D^V \max\left[\frac{2\pi}{\ln(8r_{I_n}/r_p)}, 1\right], \quad (25)$$

$$(26)$$

where $r_p = 2b$ is assumed, following [17]. The capture radii r_{I_n} and r_{V_n} , for interstitial and vacancy clusters of size n are given by:

$$r_{I_n} = \sqrt{\frac{nV_{at}}{\pi b}}, \quad (27)$$

$$r_{V_n} = (3nV_{at}/4\pi)^{1/3} + \sqrt{3}a_0/4. \quad (28)$$

A.2 Dislocation evolution details

In the evolution of the dislocation density (Equation 3) [19], the climb velocity of the dislocations is given by:

$$v_{cl} = \frac{2\pi}{b \ln R/r_c} \left[Z_D^I D_I C_I - Z_D^V D_V (C_V - C_V^D) \right], \quad (29)$$

where, C_V^D is the equilibrium concentration of vacancies near a dislocation, $C_V^D = C_V^{eq} \exp\left(\frac{\sigma V_{at}}{k_B T}\right)$ [29], where C_V^{eq} is the equilibrium vacancy concentration in the bulk, V_{at} is the atomic volume, σ is the internal stress due to pinned dislocations, $\sigma = A\mu b\sqrt{\rho_p}$, where $\rho_p = 0.1\rho$ is the pinned dislocation density and $A=0.4$. $R/r_c = 2\pi$ is taken, where R and r_c are the outer radius and core radius of the dislocations.

Furthermore, S_{BH} , the Bardeen-Herring source density is given by $S_{BH} = (\rho_p/3)^{1.5}$ and $d_{cl} = (\pi\rho)^{-1/2}$ is the distance that dislocations can travel before they annihilate [19].

A.3 Model parameters

Parameter	Unit	Value	Description	Reference
a_0	nm	0.31652	Lattice parameter	[30]
α_T	-	0.15	Taylor barrier strength	[31]
γ_b	J/m ²	0.869	GB-surface energy	[13]
δ	nm	1	grain boundary thickness	[32]
D_0^{GB}	m ² /s	0.27×10^{-4}	Self-diffusivity along grain boundaries	Estimated, using [33]
D_{I_0}	m ² /s	8.77×10^{-8}	SIA-diffusivity	[34]
D_{V_0}	m ² /s	177×10^{-8}	Vacancy diffusivity	[34]
E_I^f	eV	9.466	Formation energy SIA	[17]
E_V^f	eV	3.80	Formation energy vacancy	[17]
$E_{I_2}^b$	eV	2.12	Binding energy SIA-SIA	[17]
$E_{V_2}^b$	eV	0.6559	Binding energy V-V	[17]
E_I^m	eV	0.013	SIA migration energy	[34]
E_V^m	eV	1.66	Vacancy migration energy	[34]
K_a^A	-	5×10^7	Nucleation activation energy reduction	-
K_m	-	1490	grain boundary mobility parameter	-
K_N	#/m ² s	2.5×10^{17}	Nucleation rate constant	-
M	-	3.06	Taylor factor	[35]
μ	Pa	161×10^9	Shear modulus	[33]
Q^{GB}	J/mol	4×10^5	Activation energy for GB mobility	[33]
r_{IV}	Å	4.65	Recombination radius	[17]
V_m	m ³ /mol	9.55×10^{-6}	Molar volume	-
Z_D^I	-	1.2	SIA-dislocation bias	[17]
Z_D^V	-	1	V-dislocation bias	[17]

Table 7: Parameter values.

Simulation settings

The simulations were performed using 17 different HEMs, with the following 16 limits for the bulk stored energy density that cover a range from 1×10^2 J/m³ to 2.5×10^8 J/m³ (namely: 1×10^2 ; 1×10^3 ; 3×10^3 ; 6×10^3 ; 1×10^4 ; 5×10^4 ; 1×10^5 ; 2.5×10^5 ; 5×10^5 ; 1×10^6 ; 2.5×10^6 ; 4×10^6 ; 1×10^7 ; 3×10^7 ; 1×10^8 ; 2.5×10^8). The number of representative grains at the start of a simulation was taken to be 16. Besides those representative grains, each HEM was allowed to have up to 20 representative grains that were nucleated in the course of the simulation, so in total the maximum number of representative grains amounted up to 370, sufficient to allow for a distribution of grain sizes within each HEM. In some simulations, the maximum number of representative grains per HEM was taken to be 8 (for bulk nucleation, with $K_a^B = 10^5$ and $K_a^B = 10^6$, and for necklace nucleation with extra heating every 100 hrs) or 12 (for necklace nucleation with annealing every 500 hrs). In all simulations, the nucleation threshold was taken to be $E_{nuc}^{B,thr} = 10^6$ J/m³. In the cluster dynamics model, $N_I = N_V = 100$ is used for all simulations. The simulations that were performed in section 2.5 were performed with 20 different HEMs, using 3 extra HEM limits (namely: 1.3×10^6 , 1.6×10^6 and 2.0×10^6).

B Solution procedure

The solution procedure is based on [12], but with several modifications to account for non-isothermal loading and for multiple HEMs.

1. **Time step.** The size of the time step $\Delta t = t_{i+1} - t_i$ is calculated, where the constraints of Table 8 are taken into account.
2. **Defect evolution.** The evolution of the defect concentrations for each grain is calculated using cluster dynamics.

3. **Redistribution.** Based on E^B , the representative grains are assigned to the HEMs. If the maximum amount of representative grains in a HEM is exceeded, then the two representative grains in this HEM that are most alike (based on their bulk and surface properties E^B and E^S) are merged to form one representative grain.
4. **Nucleation.** For necklace nucleation, \dot{N}^A , r_{nuc}^A , E_{act}^A and A_{nuc} are calculated. The volume for the newly nucleated grains is delivered by all the HEMs, according to the surface fractions. Within a HEM, the nucleated volume is provided by the representative grains according to their volume fraction. In the simulations where bulk nucleation is taken into account, \dot{N}^B , r_{nuc}^B , E_{act}^B and V_{nuc} are calculated. Also for bulk nucleation, all representative grains that contribute to the nucleation volume, deliver the volume for the new nuclei according to their volume fractions. The nuclei that are formed are placed in the lowest energy HEM. A HD-daughter grain can only merge with other HD-daughter grains.
5. **Time step check.** If more grains nucleated in the previous time increment than were already present (counting nucleated grains only), then the calculations for this time increment are repeated, using a reduced time step size Δt .
6. **Grain growth.** All regular grains obtain new grain radii and new concentrations. If grains vanish, then subincrements are used to avoid negative radii.
7. **Time step check.** If the overall stored energy density of the microstructure decreased too much in a single time increment (more than 5%), then the calculations are repeated with a smaller time step size Δt .

Volume conservation during grain growth

In general, the volume change of a grain k during grain growth is calculated using Equation 7. An exception is made for grains that shrink with respect to their own HEM. If a grain k in HEM q shrinks with respect to HEM q , then the appropriate term in the summation of Equation 7 is replaced by the following:

$$\Delta V_k^q = -4\pi m \Delta t r_k^2 \phi^q \Delta E_k^q \frac{\sum_{k \in q: \Delta V_k^q > 0} \Delta V_k^q N_k}{\sum_{k \in q: \Delta V_k^q < 0} \Delta V_k^q N_k}, \quad (30)$$

to conserve the volume, after [18].

Mechanism	Rule
General	The size of the time step can increase no more than 5% with respect to the step size during the previous time increment (or, when the step size is smaller than 10 s, an increase of up to 50% is allowed).
Grain growth	No grain is allowed to growth or shrink more than 10% with respect to a HEM (unless the grain is smaller than 0.1% of the average grain volume). This is estimated based on the relative volume changes during the previous time increment.
Nucleation	The amount of nucleated grains N_{new} during a time step may not exceed the total amount of newly formed grains $N_{new,tot}$ that already exist in the microstructure. If this number is exceeded, then all events during the time increment are recalculated, using an adjusted time step size $dt \rightarrow dt \times N_{new,tot}/N_{new}$.
Temperature	During a single time increment, the temperature may increase no more than 30 K. Also, the starts and ends of the dwell times should coincide with the start/end of a time increment. Since the temperature is prescribed, these adjustments can be made at the beginning of the time increment.
Recovery	The total energy density $E = \sum_{n=1}^{n_{HEMs}} \gamma^n E^{HEM,n}$ should not decrease more than 5% during a single time increment: if $(E_{i+1} - E_i)/E_i > -0.05$, then $dt \rightarrow dt/(E_{i+1} - E_i /0.05E_i)$, where $E(i)$ is the total energy density during the previous time increment; and $E(i+1)$ the total energy density during the first try for the current time increment.

Table 8: Time step limitations.

Gibbs free energy change during nucleation

To determine the nucleation radii and activation energies for necklace nucleation and bulk nucleation, the following expressions are used:

$$\frac{\partial \Delta E}{\partial t} = \frac{\partial \Delta E}{\partial E^B} \frac{dE^B}{dt} + \frac{\partial \Delta E}{\partial r} \frac{dr}{dt} = \quad (31)$$

$$= \frac{1}{K_a^A} \left[-\frac{4\pi}{3} r^3 \frac{dE^B}{dt} - 4\pi r^2 m (E^B - E_0^B) (E - E_0^B) + 6\pi r m \gamma_b (E^B + E - 2E_0^B) - 9\pi m \gamma_b^2 \right] < 0, \quad (32)$$

for necklace nucleation, and

$$\begin{aligned} \frac{\partial \Delta E}{\partial t} &= \frac{\partial \Delta E}{\partial E^{B,HD}} \frac{dE^{B,HD}}{dt} + \frac{\partial \Delta E}{\partial r} \frac{dr}{dt} = \\ &= \frac{1}{K_a^B} \left[-\frac{4\pi}{3} r^3 \frac{dE^{B,HD}}{dt} - 4\pi r^2 m (E^{B,HD} - E_0^B) (E^{HD} - E_0^B) \right. \\ &\quad \left. + 6\pi r m \gamma_b (E^{B,HD} + \frac{4}{3} E^{HD} - \frac{7}{3} E_0^B) - 12\pi m \gamma_b^2 \right] < 0, \end{aligned} \quad (33)$$

for bulk nucleation. Here, $E^{B,HD}$ and E^{HD} are the (volume) average stored energy densities of the representative grains for which E^B exceeds the nucleation threshold energy density. As detailed in [12], the derivatives are determined numerically. The nucleated grain size is taken to be $r_{nuc} = 1.01r_0$, where r_0 denotes the largest solution to the above equations. The nucleation activation energy follows from $E_{act} = \Delta E(r^*)$, where r^* is the solution to the static case, $d\Delta E/dr = 0$.

C SRX parameter characterization

Figure 10 shows the dependence of the final average grain size and the time to complete recrystallization on the parameters K_N and K_m for a given K_a , for static recrystallization, using the microstructure parameters, process conditions and simulation settings as mentioned in section 2.5.

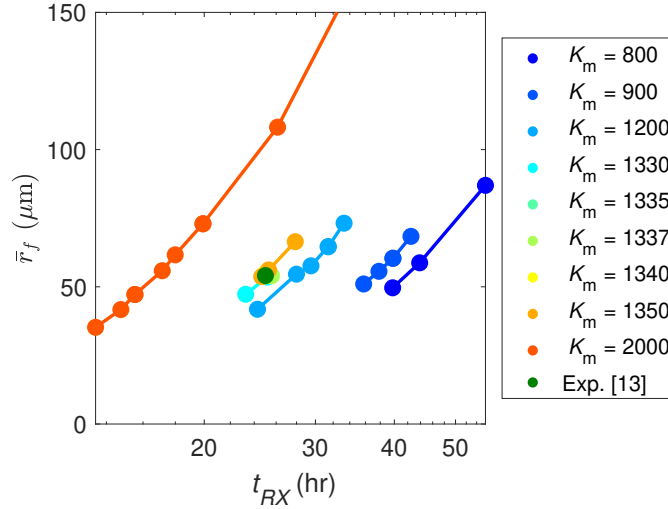


Figure 10: Final grain size \bar{r}_f after static recrystallization and time of full recrystallization t_{RX} for $K_a=3 \times 10^6$ and for various values of K_m and K_N , in comparison to the experimental result of [13].

References

- [1] H. Bolt, V. Barabash, W. Krauss, J. Linke, R. Neu, S. Suzuki, N. Yoshida, and ASDEX Upgrade Team. Materials for the plasma-facing components of fusion reactors. In: *Journal of Nuclear Materials* 329 (2004), pp. 66-73.
- [2] X. Hu, T. Koyanagi, M. Fukuda, N. A. P. Kiran Kumar, L. L. Snead, B. D. Wirth, and Y. Katoh. Irradiation hardening of pure tungsten exposed to neutron irradiation. In: *Journal of Nuclear Materials* 480 (2016), pp. 235-243.
- [3] M. Fukuda, N. A. P. Kiran Kumar, T. Koyanagi, L. M. Garrison, L. L. Snead, Y. Katoh and A. Hasegawa. Neutron energy spectrum influence on irradiation hardening and microstructural development of tungsten. In: *Journal of Nuclear Materials* 479 (2016), pp. 249-254.
- [4] G. Dini, A. Najafizadeh, R. Ueji, and S. M. Monir-Vaghefi. Improved tensile properties of partially recrystallized submicron grained TWIP steel. In: *Materials Letters* 64 (2010), pp. 15-18.
- [5] J. Reiser, M. Rieth, A. M\u00e4\u00fcslang, B. Dafferner, J. Hoffmann, T. Mrotzek, A. Hoffmann, D. E. J. Armstrong, and X. Yi. Tungsten foil laminate for structural divertor applications joining of tungsten foils. In: *Journal of Nuclear Materials* 436 (2012), pp. 47-55.
- [6] D. Terentyev, X. Xiao, A. Dubinko, A. Bakaeva, and H. Duan. Dislocation-mediated strain hardening in tungsten: thermo-mechanical plasticity theory and experimental validation. In: *Journal of the Mechanics and Physics of Solids* 85 (2015), pp. 1-15.
- [7] M. Wirtz, I. Uytendhouwen, V. Barabash, F. Escourbiac, T. Hirai, J. Linke, Th. Loewenhoff, S. Panayotis, and G. Pintsuk. Material properties and their influence on the behaviour of tungsten as plasma-facing material. In: *Nuclear Fusion* 57 (2017), pp. 1-8.

- [8] M. Wirtz, A. Kreter, J. Linke, T. Loewenhoff, G. Pintsuk, G. Sergienko, I. Steudel, B. Unterberg, and E. Wessel. High pulse number thermal shock tests on tungsten with steady state particle background. In: *Physica Scripta T170* (2017), p. 014066.
- [9] D. Scheiber, R. Pippan, P. Puschnig, and L. Romaner. Ab initio calculations of grain boundaries in bcc metals. In: *Modelling and Simulation in Materials Science and Engineering 24* (2016), p. 35013.
- [10] C. Ren, Z. Z. Fang, M. Koopman, B. Butler, J. Paramore, and S. Middlemas. Methods for improving ductility of tungsten - a review. In: *International Journal of Refractory Metals and Hard Materials 75* (2018), pp. 170-183.
- [11] A. Mannheim, J. A. W. van Dommelen, and M. G. D. Geers. Modelling recrystallization and grain growth of tungsten induced by neutron displacement defects. In: *Mechanics of Materials 123* (2018), pp. 43-58.
- [12] A. Mannheim, J. A. W. van Dommelen, and M. G. D. Geers. Long-term microstructural evolution of tungsten under heat and neutron loads. In: *ArXiv preprint* (2019). arXiv: 1901.03272.
- [13] A. Lopez. Thermal stability of warm-rolled tungsten. PhD Thesis. Technical University of Denmark, 2015.
- [14] W. V. Vaidya, and K. Ehrlich. Radiation-induced recrystallization, its cause and consequences in heavy-ion irradiated 20p cold-drawn steels of type 1.4970. In: *Journal of Nuclear Materials 113* (1983), pp. 149-162.
- [15] D. Kaoumi, A. T. Motta, and R. C. Birtcher. A thermal spike model of grain growth under irradiation. In: *Journal of Applied Physics 104* (2008), p. 073525.
- [16] A. Hardouin Duparc, C. Moingeon, N. Smetniansky-De-Grande, and A. Barbu. Microstructure modelling of ferritic alloys under high flux 1 MeV electron irradiations. In: *Journal of Nuclear Materials 302* (2002), pp. 143-155.
- [17] Y. G. Li, W. H. Zhou, R. H. Ning, L. F. Huang, Z. Zeng, and X. Ju. A cluster dynamics model for accumulation of helium in tungsten under helium ions and neutron irradiation. In: *Communications in Computational Physics 11* (2012), pp. 1547-1568.
- [18] P. Bernard, S. Bag, K. Huang, and R. E. LogÃ¶f. A two-site mean-field model of discontinuous dynamic recrystallization. In: *Materials Science and Engineering A 528* (2011), pp. 7357-7367.
- [19] R. E. Stoller. Modeling dislocation evolution in irradiated alloys. In: *Metallurgical Transactions A 21* (1990), pp. 1829-1837.
- [20] T. Jourdan. Influence of dislocation and dislocation loop biases on microstructures simulated by rate equation cluster dynamics. In: *Journal of Nuclear Materials 467* (2015), pp. 286-301.
- [21] W. Setyawan, G. Nandipati, K.J. Roche, H. L. Heinisch, B. D. Wirth, and R. J. Kurtz. Displacement cascades and defects annealing in tungsten, Part I: defect database from molecular dynamics simulations. In: *Journal of Nuclear Materials 462* (2015), pp. 329-337.
- [22] F. Gao, and D. J. Bacon. Molecular dynamics study of displacement cascades in Ni3Al II. Kinetics, disordering and atomic mixing. In: *Philosophical Magazine A 71* (1995), pp. 65-84.
- [23] A. E. Sand, J. ByggmÃ¶star, A. Zitting, and K. Nordlund. Defect structures and statistics in overlapping cascade damage in fusion-relevant bcc metals. In: *Journal of Nuclear Materials 511* (2018), pp. 64-74.
- [24] M. J. Norgett, M. T. Robinson, and I. M. Torrens. A proposed method of calculating displacement dose rates. In: *Nuclear Engineering and Design 33* (1975), pp. 50-54.

- [25] K. Nordlund, S. J. Zinkle, A. E. Sand, F. Granberg, R. S. Averback, R. E. Stoller, T. Suzudo, L. Malerba, F. Banhart, W. J. Weber, F. Willaime, S. L. Dudarev, and D. Simeone. Primary radiation damage: A review of current understanding and models. In: *Journal of Nuclear Materials* 512 (2018), pp. 450-479.
- [26] T. Tanno, A. Hasegawa, J. -C. He, M. Fujiwara, S. Nogami, M. Satou, T. Shishido, and K. Abe. Effects of transmutation elements on neutron irradiation hardening of tungsten. In: *Materials Transactions* 48 (2007), pp. 2399-2402.
- [27] M. Fukuda, T. Tanno, S. Nogami, and A. Hasegawa. Effects of Re content and fabrication process on microstructural changes and hardening in neutron irradiated tungsten. In: *Materials Transactions* 53 (2012), pp. 2145-2150.
- [28] D. G. Cram, H. S. Zurob, Y. J. M. Brechet, and C. R. Hutchinson. Modelling discontinuous dynamic recrystallization using a physically based model for nucleation. In: *Acta Materialia* 57 (2009), pp. 5218-5228.
- [29] G. S. Was. *Fundamentals of Radiation Materials Science*. Springer, 2007, p. 839. isbn: 9783540494713.
- [30] E. Lassner, and W. -D. Schubert. *Tungsten properties, chemistry, technology of the element, alloys, and chemical compounds*. Springer Science & Business Media, 2012.
- [31] K. M. Davoudi, and J. J. Vlassak. Dislocation Evolution During Plastic Deformation: Equations vs. Discrete Dislocation Simulations. In: *arXiv preprint* (2014), pp. 1-23. arXiv: 1408.6609.
- [32] J. Favre, D. Fabregue, D. Piot, N. Tang, Y. Koizumi, E. Maire, and A. Chiba. Modeling grain boundary motion and dynamic recrystallization in pure metals. In: *The Minerals, Metals and Materials Society* 44 (2013), pp. 5861-5875.
- [33] E. Lassner, and W. Schubert. *The element tungsten*. Springer, 1999.
- [34] T. Faney. Numerical simulations of tungsten under helium irradiation. PhD thesis. University of California, Berkeley, 2013.
- [35] R. E. Stoller, and S. J. Zinkle. On the relationship between uniaxial yield strength and resolved shear stress in polycrystalline materials. In: *Journal of Nuclear Materials* 283-287 (2000), pp. 349-352.